Article

Torque Calculation and Dynamical Response in Halbach Array Coaxial Magnetic Gears through a Novel Analytical 2D Model

Panteleimon Tzouganakis [1,*], Vasilios Gakos [2], Christos Kalligeros [2], Christos Papalexis [1], Antonios Tsolakis [1] and Vasilios Spitas [2]

1   Laboratory of Machine Elements and Vehicles, University of West Attica, 250 Thivon & P. Ralli, 12244 Egaleo, Greece; chpapalexis@uniwa.gr (C.P.); adtsolakis@uniwa.gr (A.T.)
2   Laboratory of Machine Design, National Technical University of Athens, 9 Iroon Polytechniou, 15780 Zografou, Greece; vgakos@mail.ntua.gr (V.G.); ckalligeros@mail.ntua.gr (C.K.); vspitas@mail.ntua.gr (V.S.)
*   Correspondence: ptzouganakis@uniwa.gr

Abstract: Coaxial magnetic gears have piqued the interest of researchers due to their numerous benefits over mechanical gears. These include reduced noise and vibration, enhanced efficiency, lower maintenance costs, and improved backdrivability. However, their adoption in industry has been limited by drawbacks like lower torque density and slippage at high torque levels. This work presents an analytical 2D model to compute the magnetic potential in Halbach array coaxial magnetic gears for every rotational angle, geometry configuration, and magnet specifications. This model calculates the induced torques and torque ripple in both rotors using the Maxwell Stress Tensor. The results were confirmed through Finite Element Analysis (FEA). Unlike FEA, this analytical model directly produces harmonics values, leading to faster computational times as it avoids torque calculations at each time step. In a case study, a standard coaxial magnetic gear was compared to one with a Halbach array, revealing a 14.3% improvement in torque density and a minor reduction in harmonics that cause torque ripple. Additionally, a case study was conducted to examine slippage in both standard and Halbach array gears during transient operations. The Halbach array coaxial magnetic gear demonstrated a 13.5% lower transmission error than its standard counterpart.

Keywords: coaxial magnetic gear; Halbach array; analytical torque calculation; dynamical response; slip effect; torque ripple

1. Introduction

Magnetic gears (MGs) possess significant advantages compared to mechanical gears such as a lower level of noise and vibration, backdrivability, lower maintenance cost and higher reliability [1] due to the absence of contact between the moving parts. Due to the above advantages, MGs have been used in several power transmission applications such as in aircraft mechanical transmissions [2–4], electric vehicles [5], wave energy conversion [6–8] and space applications [9]. However, the lower torque density (typically one order of magnitude [1]) of the MGs compared to mechanical gears and rare-earth materials scarcity prevents the wide adoption of these drives in the industry. To overcome this issue, a significant number of topologies of MGs have been proposed by researchers while the modelling and optimization of MGs have been extensively discussed in the literature.

A promising topology for the increase in the torque density in MG drives is the coaxial magnetic gear (CMG) arrangement proposed in 2001 by Atallah et al. [10]. CMG performance can be further improved if the permanent magnets (PMs) are placed in a specific arrangement called Halbach array [8,11–13]. Halbach arrays can create a strong magnetic field [14] due to their inherent capability to generate a one-sided magnetic field [15]. The Halbach array CMG (HAL-CMG) drive has a higher torque density, superior dynamical response under load and good self-shielding magnetization [16–19]. However, these drives

insert further parameters in the optimization process, making the problem of increasing the torque density computationally intensive. Therefore, an analytical calculation of the torque would significantly reduce the computational cost required to achieve optimal torque density for a given configuration of the HAL-CMG drive and in general would facilitate the design of application-specific HAL-CMG drives. The magnetic field is calculated analytically through a 2D model developed by Jian et al. [20] assuming equipotential iron pole pieces. The induced torques in the inner and outer rotor of the CMG are calculated from the Maxwell Stress Tensor [21–24]. Thus, the calculation of the dynamical response of the CMG drive during transient operation of the CMG drive would require the calculation of the induced torque in every time step, increasing significantly the computational cost. Recently, a new methodology [25] developed by the authors proposed an analytical method of calculating the torque in every angle of rotation of the CMG rotors. The methodology for obtaining analytical solutions for the induced torques is similar to the case of axial magnetic gears [26]. With the model developed in [25], the torque is calculated analytically in only one position and through an analytical formulation, can be obtained in every other angle of rotation. Therefore, the computational cost required for the calculation of the dynamical response and the resulting slippage of the CMG drive during transient operation is significantly reduced.

In the present study, a novel analytical 2D model for the calculation of the magnetic potential of the HAL-CMG drive has been derived. The applied torque on the two rotors and the torque ripple were calculated analytically using the Maxwell Stress Tensor. Therefore, the dynamical response of the HAL-CMG drive can be determined with a single torque calculation at a single position. A case study was performed for a four-pole-pair inner rotor and a ten-pole-pair outer rotor in a standard CMG and an optimized HAL-CMG with the same geometrical and parameters of the PMs. The stall torque and the amplitude of the harmonics contributing to the torque ripple were calculated and compared for the two drives. In addition, the obtained torques were verified with Finite Element Analysis (FEA). The stall torque of the HAL-CMG was 14.3% higher than the standard CMG's while the amplitudes of the torque-contributing harmonics which generate torque ripple were slightly reduced. Finally, a case study of transient operation was performed in order to investigate the dynamical response of the two types of CMG drives and determine the transmission error, which was found to be 13.5% lower for the HAL-CMG. Therefore, as expected, with the use of HAL-CMG the stall torque is increased compared to the standard CMG drive, while a better dynamical response is achieved during transient operation without compromising the other operational characteristics.

2. Analytical Modelling

2.1. Magnetic Potential Calculation

The three components of the HAL-CMG are: the inner rotor, the outer rotor and the flux modulator ring. As shown in Figure 1, $r_1, r_2, r_3, r_4, r_5, r_6, r_{out}$ are the radii of the inner iron yoke, the inner PMs, the inner and the outer side of the modulator ring, the outer PMs, the outer iron yoke and the external side of the HAL-CMG, respectively, while δ is the angle of each ferromagnetic segment. The different colors of the PMs represent the different orientations of the magnets.

The calculation of the scalar magnetic potential in standard CMGs has been developed by Jian et al. [20]. In the present research, an analytical 2D model for the calculation of the magnetic potential for the HAL-CMG is proposed. The magnetic field of the HAL-CMG is obtained as a superposition of the magnetic fields generated by the PMs of the inner and outer rotor separately. In order to obtain an analytical solution, infinite permeability of the iron yokes and the ferromagnetic segments is assumed.
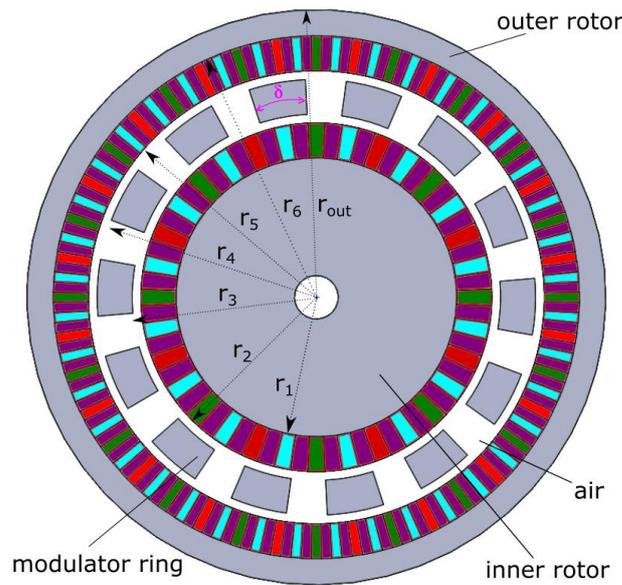
Figure 1. Halbach array coaxial magnetic gear.

Figure 2, depicts a linear analogue of the HAL-CMG shown in Figure 1 with PMs only on the inner rotor. Furthermore, $\alpha_h, \beta_h, \gamma_h, \psi$ are the PMs angles of the Halbach array.
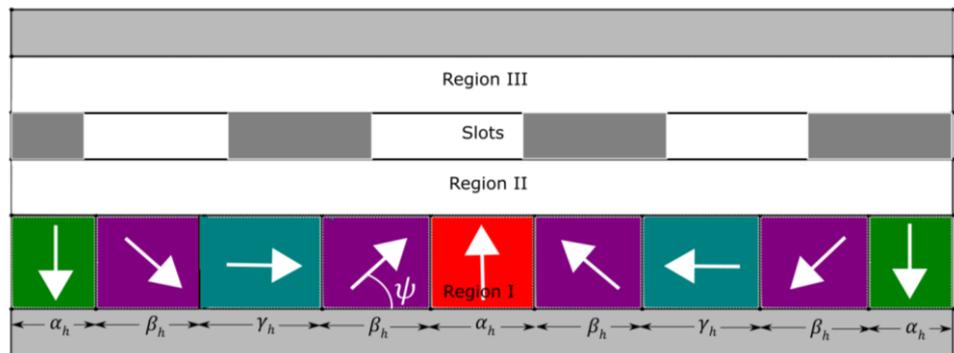

Figure 2. Linear analogue of a section of HAL-CMG (one pole-pair).

The governing equations for each region of Figure 2, are [20,25]:

$$\nabla^2 \varphi^I(r,\theta) = \frac{\text{div}\boldsymbol{M}}{\mu_r}, \text{ in Region I} \tag{1}$$

$$\nabla^2 \varphi^{II,III}(r,\theta) = 0, \text{ in Regions II, III} \tag{2}$$

$$\nabla^2 \varphi^S(r,\theta) = 0, \text{ in the slots} \tag{3}$$

where φ is the scalar magnetic potential for each region, and μ_r is the relative permeability of the PMs.

The solution of Equation (2) for *Regions II, III* is:

$$\varphi^{II}(r,\theta) = \sum_{n=1}^{\infty} \left[\left(E_n r^n + F_n r^{-n} \right) \cos(n\theta) + \left(G_n r^n + H_n r^{-n} \right) \sin(n\theta) \right] + E_0 \ln r + F_0 \tag{4}$$

$$\varphi^{III}(r,\theta) = \sum_{n=1}^{\infty} \left[\left(I_n r^n + J_n r^{-n} \right) \cos(n\theta) + \left(K_n r^n + L_n r^{-n} \right) \sin(n\theta) \right] + I_0 \ln r + J_0 \tag{5}$$

In order to obtain the solution of Equation (1), the magnetization vector $\boldsymbol{M}$ of the HAL-CMG has to be written in the form of Fourier Series as follows:

$$\boldsymbol{M} = M_r\boldsymbol{r} + M_\theta\boldsymbol{\theta} \tag{6}$$

where M_r and M_θ are the radial and tangential components of magnetization, respectively, presented in Figures 3 and 4, while $\boldsymbol{r}$ and $\boldsymbol{\theta}$ are unit vectors.
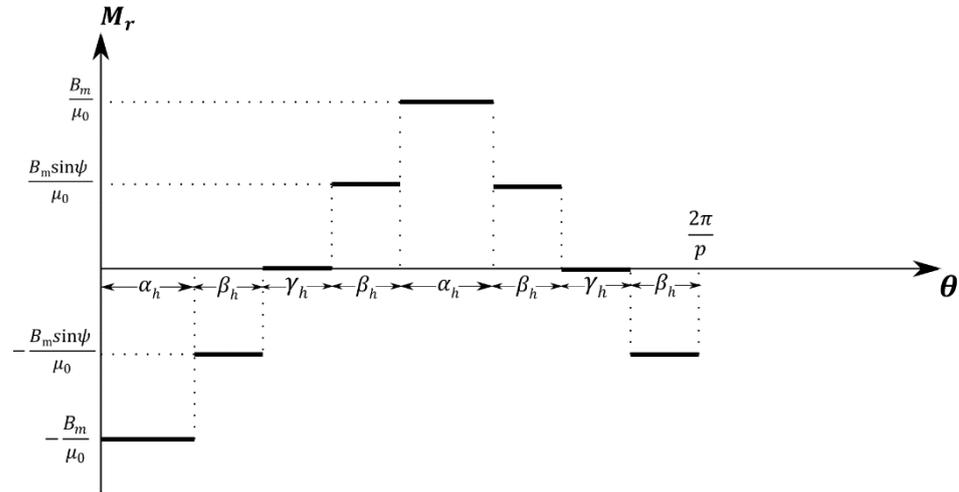

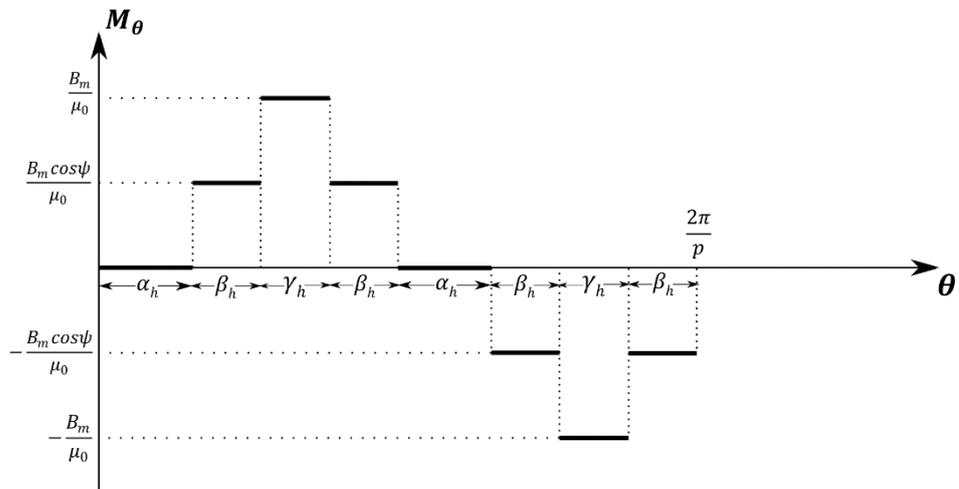**Figure 3.** Radial magnetization distribution in Region I.

Figure 4. Tangential magnetization distribution in Region I.

Where B_m is the residual magnetism of the PM, and $\alpha_h, \beta_h, \gamma_h, \psi$ are the PMs angles, while p is the number of pole pairs of the Halbach array, as shown in Figure 2. The radial magnetization, M_r, can be written as:

$$M_r(\theta) = \sum_{k=1}^{\infty} a_k\cos(kp(\theta - \theta_0)) + b_k\sin(kp(\theta - \theta_0)) \tag{7}$$

where θ_0 is the angle of rotation of the inner rotor

The tangential magnetization, M_θ, can be written as:

$$M_\theta(\theta) = \sum_{k=1}^{\infty} d_k\cos(kp(\theta - \theta_0)) + e_k\sin(kp(\theta - \theta_0)) \tag{8}$$

where the Fourier coefficients a_k, b_k, d_k and e_k are given as a function of $\alpha_h, \beta_h, \gamma_h, \psi$ in Appendix A.

As a consequence, the special solution of Equation (1) will have the following form:

$$
\begin{aligned}
\varphi_s(r,\theta) = \sum_{n=1}^{\infty} \{ W_n(r)[(a_k\cos(n\theta_0) - b_k\sin(n\theta_0) + d_k n\sin(n\theta_0) \\
+ e_k n\cos(n\theta_0))\cos(n\theta) + (a_k\sin(n\theta_0) + b_k\cos(n\theta_0) \\
- d_k\, n\cos(n\theta_0) + e_k\, n\sin(n\theta_0))\sin(n\theta)] \}
\end{aligned}
\tag{9}
$$

where:

$$
W_n(r) = \begin{cases} \dfrac{r}{\mu_r(1-n^2)}, & if\ n = pk \\[2mm] \dfrac{rlnr}{2\mu_r}, & if\ n = pk = 1 \\[2mm] 0, & if\ n \neq pk \end{cases}
\tag{10}
$$

and $k = \{1, 2, 3, \ldots\}$.

Therefore, the general solution of Equation (1) is:

$$
\begin{aligned}
\varphi^I(r,\theta) = \sum_{n=1}^{\infty} [(A_n r^n + B_n r^{-n} + W_n(r)(a_k\cos(n\theta_0) - b_k\sin(n\theta_0) \\
+ d_k\, n\sin(n\theta_0) + e_k\, n\cos(n\theta_0)))\cos(n\theta) + (C_n r^n + D_n r^{-n} + W_n(r)(a_k\sin(n\theta_0) + b_k\cos(n\theta_0) \\
- d_k\, n\cos(n\theta_0) + e_k\, n\sin(n\theta_0)))\sin(n\theta)] + A_0 lnr + B_0
\end{aligned}
\tag{11}
$$

The solution of the Equation (3) is:

$$
\varphi^S_j(r,\theta) = \frac{\varphi^F_{j+1} - \varphi^F_j}{\gamma}(\theta - \alpha_j) + \varphi^F_j + \sum_{n=1}^{\infty} \left[\left(X_{jn} r^{\frac{n\pi}{\gamma}} + Y_{jn} r^{-\frac{n\pi}{\gamma}} \right) \sin\left(\frac{n\pi}{\gamma}(\theta - \alpha_j) \right) \right]
\tag{12}
$$

where φ^F_j is the magnetic potential of the jth ferromagnetic segment, γ is the central slot angle and α_j is the left angle of each ferromagnetic segment.

The unknown coefficients: $A_n, B_n, C_n, D_n, E_n, F_n, G_n, H_n, I_n, J_n, K_n, L_n, A_0, B_0, E_0, F_0, I_0, J_0, X_{jn}, Y_{jn}, \varphi^F_j$ of Equations (4), (5), (11) and (12), can be determined from the following boundary conditions [20,25].

1. The magnetic potential in the radii r_1 and r_6 should be zero ($\varphi^I_{r_1} = 0, \varphi^I_{r_6} = 0$).
2. The continuity of the magnetic potential and the continuity of the radial flux density (derivative of the magnetic potential) between adjacent regions should be satisfied.
3. The flux flowing from the inside surface of the modulator ring should be equal to the flux flowing to the outside surface of the modulator ring.
4. The flux flowing into the ferromagnetic segment should be equal to the flux flowing out.

Therefore, from the boundary conditions, a system of linear equations is derived that can be solved with the Gauss method, and consequently, the magnetic potential induced by the inner rotor PMs can be calculated.

Similarly, the magnetic potential generated from the outer rotor PMs can be calculated.

As a consequence, the radial and tangential magnetic flux in the HAL-CMG (after the superposition of the magnetic potentials induced by the PMs of the inner and outer rotor) is:

$$
B_r = -\mu_0 \frac{\partial \varphi}{\partial r}
\tag{13A}
$$

$$
B_\theta = -\frac{\mu_0}{r} \frac{\partial \varphi}{\partial \theta}
\tag{13B}
$$

2.2. Analytical Torque Calculation of HAL-CMG

Similarly to the standard CMG, the torque can be calculated analytically using the Maxwell Stress Tensor [25]. Therefore, the torque at the two rotors can be calculated from Equations (14) and (15).

$$M_{in}(r_2) = \sum_{k=1}^{\infty} \xi_{(2k-1)p_{in},in}\sin[(2k-1)p_{in}\theta_{in} + (2k-1)p_{out}\theta_{out}] \tag{14}$$

$$M_{out}(r_5) = \sum_{k=1}^{\infty} \xi_{(2k-1)p_{out},out}\sin[(2k-1)p_{in}\theta_{in} + (2k-1)p_{out}\theta_{out}] \tag{15}$$

where $\xi_{(2k-1)p_{in},in}$ and $\xi_{(2k-1)p_{out},out}$ are the amplitudes of the torque-contributing harmonic terms in the inner and outer rotor, respectively, which can be calculated analytically from the coefficients $A_n, B_n, C_n, D_n, E_n, F_n, G_n, H_n, I_n, J_n, K_n, L_n, A_0, B_0, E_0, F_0, I_0, J_0, X_{jn}, Y_{jn}$ as shown in [25].

2.3. Dynamical System Equations

The system of HAL-CMG dynamical equations can be expressed as:

$$I_{in}\ddot{\theta}_{in} + \sum_{k=1}^{\infty} \xi_{(2k-1)p_{in},in}\sin[(2k-1)p_{in}\theta_{in} + (2k-1)p_{out}\theta_{out}] = T_{in} \tag{16}$$

$$I_{out}\ddot{\theta}_{out} + \sum_{k=1}^{\infty} \xi_{(2k-1)p_{out},out}\sin[(2k-1)p_{in}\theta_{in} + (2k-1)p_{out}\theta_{out}] = -T_{out} \tag{17}$$

where I_{in}, T_{in}, I_{out} and T_{out} are the moments of inertia and the external applied torque at the inner and outer rotors, respectively [25]. Since the aim of the dynamical response model is to determine the slippage in the HAL-CMG and the maximum transmission error during acceleration/deceleration, mechanical losses and friction are not considered in the present study.

3. Results

3.1. Torque Calculation, Optimization of HAL-CMG and Comparison with Standard CMG

To illustrate the improvement in the torque density that is achieved with the use of HAL-CMG drives, a case study was performed for a standard CMG and an HAL-CMG drive with the same geometrical and constitutive parameters of the PMs, as is presented in Table 1. The iron yokes and the modulator ring of the HAL-CMG are pure iron, while the PMs are NdFeB (N52 grade).

Table 1. Geometrical Parameters of the CMG.

p_{in}	4
p_{out}	10
r_1 [mm]	80
r_2 [mm]	100
r_3 [mm]	105
r_4 [mm]	125
r_5 [mm]	130
r_6 [mm]	150
r_{out} [mm]	170
L [mm]	100
δ [deg]	15
B_r [T]	1.44
I_{in} [kgm^2]	0.1178
I_{out} [kgm^2]	0.0904

The parameters of the Halbach array for the inner and outer rotor (described in Figure 2) resulted from optimization of the stall torque and are presented in Table 2. The optimization process did not require an advanced technique since with the proposed model, the stall torque can be obtained analytically for any Halbach array arrangement in the two rotors with a low computational cost. It should be noted that the optimal arrangement of the outer rotor, in the performed case study, is the standard CMG, since the angles β_h and γ_h of the outer rotor are equal to zero.

Table 2. Parameters of the HAL-CMG drive.

Inner Rotor	
α_h [deg]	18
β_h [deg]	9
γ_h [deg]	9
ψ [deg]	60
Outer Rotor	
α_h [deg]	18
β_h [deg]	–
γ_h [deg]	–
ψ [deg]	–

In Figure 5, the applied torque in the two rotors is presented for the two drives for the case of fixed inner rotor and rotating outer rotor.
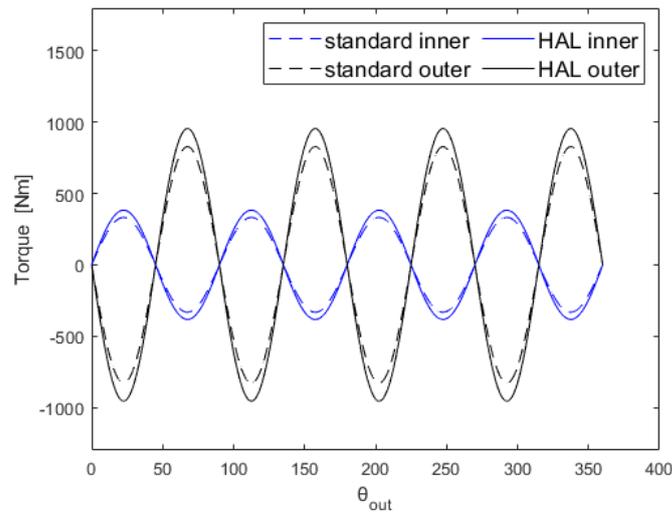
Figure 5. Comparison of the torques applied on the inner and outer rotor in the standard and the HAL-CMG.

It can be observed that there is a significant improvement in the torque density with the use of HAL-CMG. More specifically, the stall torque of the HAL-CMG was 14.3% higher than the standard CMG, which is coherent with experimental results [1].

In Figure 6, the induced torques in the two rotors of the HAL-CMG were verified with FEA (ANSYS Maxwell). The adopted mesh type used in the FEA model is triangles with an automatic meshing method that refines the mesh until convergence. A difference of 1–1.5% was observed between the analytical and FEA model; however, the computational cost was significantly lower. Therefore, with the developed analytical model an accurate and fast calculation of the torque in the two rotors of the HAL-CMG is achieved. Furthermore, with the developed model, the torque ripple generated from the torque-contributing harmonics can be determined, a result that cannot immediately be obtained from FEA since only the resulting torque is calculated (sum of the contributing harmonics). In order to calculate the torque ripple from FEA, it is necessary to perform a Fourier transform. The process would require additional computational time and several FEA simulations at different angles of rotation, while with the analytical model, a single calculation is sufficient to determine the torque ripple.
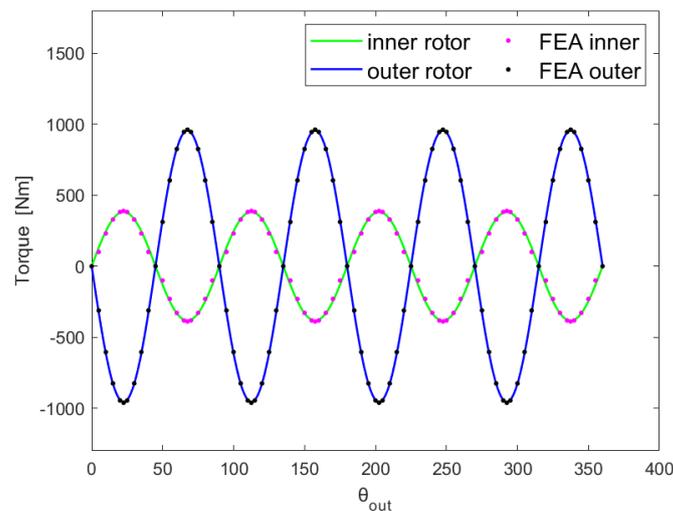

Figure 6. Torque in the two rotors of the HAL-CMG as calculated using the analytical model and FEA.

The amplitudes of the torque-contributing harmonic terms of the two rotors are presented in Table 3.

Table 3. Amplitude of contributing harmonics.

Amplitude of Inner Rotor Harmonic (Nm)			Amplitude of Outer Rotor Harmonic (Nm)		
	Standard CMG	**HAL-CMG**		**Standard CMG**	**HAL-CMG**
ξ_4	333.81	381.89	ξ_{10}	832.98	952.95
ξ_{12}	1.25	1.09	ξ_{30}	3.26	2.88
ξ_{20}	0.02	0.001	ξ_{50}	0.05	0.002

Due to the higher harmonics, torque ripple is observed in both drives. The torque ripple of the HAL-CMG is 0.3%, which is slightly lower than the torque ripple observed in the standard CMG drive. Therefore, with the use of HAL-CMG, the stall torque is increased compared to the standard CMG drive without comprising the other operational characteristics.

3.2. Dynamical Response of HAL-CMG Drive

The dynamical response of the HAL-CMG drive is determined from Equations (16) and (17) [25]. In the performed case study a defined velocity profile of the inner rotor was considered, as described in Table 4 and Figure 7. Furthermore, an external load (T_{out}) of 250 Nm was applied at the outer rotor.

Table 4. Inner rotor velocity for the performed case study.

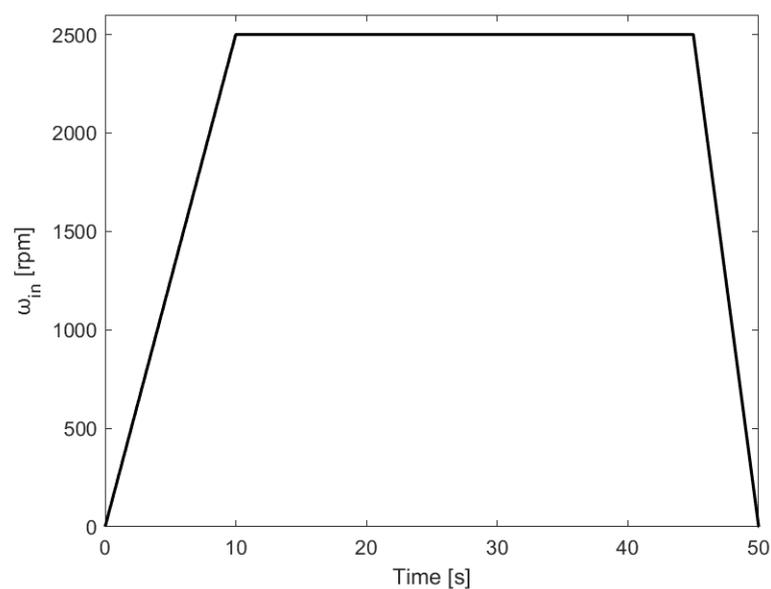| Time [s]	Velocity of Inner Rotor [rpm]
0	0
10	2500
45	2500
50	0

Figure 7. Velocity profile of the inner rotor.

The transmission error is obtained from the difference between the ideal (according to the nominal gear ratio) and the real position of the outer rotor, as obtained from Equations (16) and (17). The transmission error of the standard CMG and the HAL-CMG is compared for the performed case study. For reasons of clarity, only the envelope of the transmission error is presented in Figure 8.
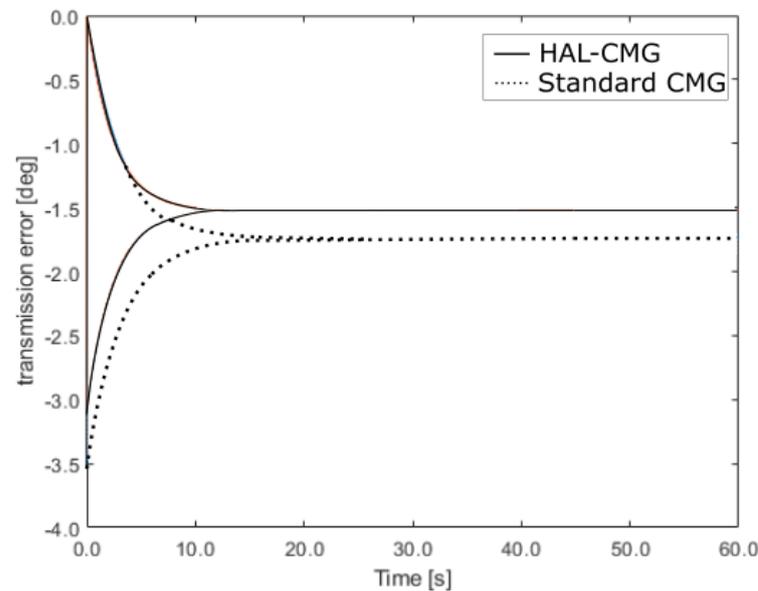

Figure 8. Envelope of transmission error of standard and HAL-CMG in the applied case study.

It can be observed that there is a significant decrease in the transmission error of the HAL-CMG in comparison to the standard CMG drive, as the maximum of the transmission error for the HAL-CMG is 13.5% lower, a result that can be attributed to the higher stall torque of the HAL-CMG. Overall, the HAL-CMG drive has higher torque density and superior dynamical response in comparison to the standard CMG drive, which is in accordance with other results in the literature [16–19].

4. Conclusions

In the present research, a novel analytical 2D model was developed for the calculation of the magnetic potential of HAL-CMGs for every angle of rotation, geometry configuration and magnet parameter. The applied torque in the two rotors was calculated analytically using the Maxwell Stress Tensor. The induced torques in the two rotors of the HAL-CMG were verified with FEA. A case study was performed for a standard CMG and an optimized HAL-CMG with the same geometrical and constitutive parameters of the PMs. The stall torque of the HAL-CMG was improved by 14.3%. In addition, the torque ripple with the use of Halbach arrays was slightly reduced compared to the standard CMG. Finally, a case study of transient operation was performed in order to investigate the dynamical response of the two types of CMG drives and determine the transmission error. The transmission error of the HAL-CMG was 13.5% lower than the standard CMG, a result that can be attributed to its higher stall torque. Therefore, from the performed case study, it can be observed that the HAL-CMG offers a significant increase in torque density, a better dynamical response and a reduction in the transmission error, which is in accordance with other results in the literature. The developed model could be a valuable design tool for the optimization and the dynamical response calculation of HAL-CMGs, since the applied torque in the two rotors can be calculated analytically, thus significantly reducing the computational cost. Furthermore, the torque ripple of the HAL-CMG due to the torque-contributing harmonics can be calculated analytically, a result that cannot immediately be obtained from FEA

since a Fourier transform is required that would increase the computational cost and FEA simulations.

Nomenclature

μ_0	magnetic permeability of free space	[H/m]
μ_r	relative magnetic permeability	-
p	number of pole pairs	-
L	width of the coaxial gear	[m]
N	number of ferromagnetic segments	-
γ	central slot angle	[rad]
δ	central ferromagnetic segment angle	[deg]
Subscripts		
in	inner rotor	
out	outer rotor	
r	radial direction	
θ	tangential direction	

Appendix A

The Fourier coefficients a_k, b_k, d_k and e_k for the calculation of the radial and tangential magnetization are given as a function of the Halbach array parameters $\alpha_h, \beta_h, \gamma_h, \psi$ as follows:

$$a_k = \frac{B_m}{\pi\mu_0 k}[-sin(kp\alpha_h) - sin\psi(\sin(kp(\alpha_h + \beta_h)) - \sin(kp\alpha_h))$$
$$+sin\psi(\sin(kp(\alpha_h + 2\beta_h + \gamma_h)) - \sin(kp(\alpha_h + \beta_h + \gamma_h))) + \sin(kp(2\alpha_h + 2\beta_h + \gamma_h))$$
$$- \sin(kp(\alpha_h + 2\beta_h + \gamma_h)) + sin\psi(\sin(kp(2\alpha_h + 3\beta_h + \gamma_h)) - \sin(kp(2\alpha_h + 2\beta_h + \gamma_h)))$$
$$-sin\psi(\sin(kp(2\alpha_h + 4\beta_h + 2\gamma_h)) - \sin(kp(2\alpha_h + 3\beta_h + 2\gamma_h)))]$$

$$b_k = -\frac{B_m}{\pi\mu_0 k}[-cos(kp\alpha_h) - \cos(0)$$
$$-sin\psi(\cos(kp(\alpha_h + \beta_h)) - \cos(kp\alpha_h)) + sin\psi(\cos(kp(\alpha_h + 2\beta_h + \gamma_h)) - \cos(kp(\alpha_h + \beta_h + \gamma_h)))$$
$$+\cos(kp(2\alpha_h + 2\beta_h + \gamma_h)) - \cos(kp(\alpha_h + 2\beta_h + \gamma_h))$$
$$+sin\psi(\cos(kp(2\alpha_h + 3\beta_h + \gamma_h)) - \cos(kp(2\alpha_h + 2\beta_h + \gamma_h)))$$
$$-sin\psi(\cos(kp(2\alpha_h + 4\beta_h + 2\gamma_h)) - \cos(kp(2\alpha_h + 3\beta_h + 2\gamma_h)))]$$

$$d_k = \frac{B_m}{\pi\mu_0 k}[cos\psi(\sin(kp(\alpha_h + \beta_h)) - \sin(kp\alpha_h))$$
$$+\sin(kp(\alpha_h + \beta_h + \gamma_h)) - \sin(kp(\alpha_h + \beta_h))$$
$$+cos\psi(\sin(kp(\alpha_h + 2\beta_h + \gamma_h)) - \sin(kp(\alpha_h + \beta_h + \gamma_h)))$$
$$-cos\psi(\sin(kp(2\alpha_h + 3\beta_h + \gamma_h)) - \sin(kp(2\alpha_h + 2\beta_h + \gamma_h))) - \sin(kp(2\alpha_h + 3\beta_h + 2\gamma_h))$$
$$-\sin(kp(2\alpha_h + 3\beta_h + \gamma_h)) - cos\psi(\sin(kp(2\alpha_h + 4\beta_h + 2\gamma_h)) - \sin(kp(2\alpha_h + 3\beta_h + 2\gamma_h)))$$

$$e_k = -\frac{B_m}{\pi\mu_0 k}[cos\psi(\cos(kp(\alpha_h + \beta_h)) - \cos(kp\alpha_h))$$
$$+\cos(kp(\alpha_h + \beta_h + \gamma_h)) - \cos(kp(\alpha_h + \beta_h))$$
$$+cos\psi(\cos(kp(\alpha_h + 2\beta_h + \gamma_h)) - \cos(kp(\alpha_h + \beta_h + \gamma_h)))$$
$$-cos\psi(\cos(kp(2\alpha_h + 3\beta_h + \gamma_h)) - \cos(kp(2\alpha_h + 2\beta_h + \gamma_h)))$$
$$-\cos(kp(2\alpha_h + 3\beta_h + 2\gamma_h)) - \cos(kp(2\alpha_h + 3\beta_h + \gamma_h))$$
$$-cos\psi(\cos(kp(2\alpha_h + 4\beta_h + 2\gamma_h)) - \cos(kp(2\alpha_h + 3\beta_h + 2\gamma_h)))$$

References

1. Wang, Y.; Filippini, M.; Bianchi, N.; Alotto, P. A review on magnetic gears: Topologies, computational models, and design aspects. *IEEE Trans. Ind. Appl.* **2019**, *55*, 4557–4566. [CrossRef]
2. Ruiz-Ponce, G.; Arjona, M.A.; Hernandez, C.; Escarela-Perez, R. A Review of Magnetic Gear Technologies Used in Mechanical Power Transmission. *Energies* **2023**, *16*, 1721. [CrossRef]
3. Scheidler, J.J.; Asnani, V.M.; Tallerico, T.F. NASA's magnetic gearing research for electrified aircraft propulsion. In Proceedings of the AIAA/IEEE Electric Aircraft Technologies Symposium (EATS), Cincinnati, OH, USA, 9–11 July 2018; pp. 1–12.
4. Tallerico, T.F.; Cameron, Z.A.; Scheidler, J.J.; Hasseeb, H. Outer stator magnetically-geared motors for electrified urban air mobility vehicles. In Proceedings of the AIAA/IEEE Electric Aircraft Technologies Symposium (EATS), Virtual Event, 24–28 August 2020; pp. 1–25.
5. Chau, K.T.; Zhang, D.; Jiang, J.Z.; Liu, C.; Zhang, Y.J. Design of a magnetic-geared outer-rotor permanent-magnet brushless motor for electric vehicles. *IEEE Trans. Magn.* **2007**, *43*, 2504–2506. [CrossRef]
6. McGilton, B.; Crozier, R.; McDonald, A.; Mueller, M. Review of magnetic gear technologies and their applications in marine energy. *IET Renew. Power Gener.* **2018**, *12*, 174–181. [CrossRef]
7. Johnson, M.; Gardner, M.C.; Toliyat, H.A.; Englebretson, S.; Ouyang, W.; Tschida, C. Design, construction, and analysis of a large-scale inner stator radial flux magnetically geared generator for wave energy conversion. *IEEE Trans. Ind. Appl.* **2018**, *54*, 3305–3314. [CrossRef]
8. Baninajar, H.; Modaresahmadi, S.; Wong, H.Y.; Bird, J.; Williams, W.; Dechant, B. Designing a Halbach rotor magnetic gear for a marine hydrokinetic generator. *IEEE Trans. Ind. Appl.* **2022**, *58*, 6069–6080. [CrossRef]
9. Esnoz-Larraya, J.; Valiente-Blanco, I.; Cristache, C.; Sanchez-Garcia-Casarrubios, J.; Rodriguez-Celis, F.; Diez-Jimenez, E.; Perez-Diaz, J.L. Optimagdrive: Highperformance magnetic gears development for space applications. In Proceedings of the ESMATS, Hatfield, UK, 20–22 September 2017.
10. Atallah, K.; Howe, D. A novel high-performance magnetic gear. *IEEE Trans. Magn.* **2001**, *37*, 2844–2846. [CrossRef]
11. Jian, L.; Chau, K.T. A coaxial magnetic gear with Halbach permanent-magnet arrays. *IEEE Trans. Energy Convers.* **2010**, *25*, 319–328. [CrossRef]
12. Wong, H.Y.; Bird, J.Z.; Barnett, D.; Williams, W. A high torque density Halbach rotor coaxial magnetic gear. In Proceedings of the 2019 IEEE International Electric Machines & Drives Conference (IEMDC), San Diego, CA, USA, 12–15 May 2019; pp. 233–239.
13. Cameron, Z.A.; Tallerico, T.; Scheidler, J. Lessons learned in fabrication of a high-specific-torque concentric magnetic gear. In Proceedings of the Vertical Flight Society 75th Annual Forum & Technology Display, Philadelphia, PA, USA, 13–16 May 2019.
14. Jiang, Y.; Deng, Y.; Zhu, P.; Yang, M.; Zhou, F. Optimization on size of Halbach array permanent magnets for magnetic levitation system for permanent magnet Maglev train. *IEEE Access* **2021**, *9*, 44989–45000. [CrossRef]
15. Hilton, J.E.; McMurry, S.M. An adjustable linear Halbach array. *J. Magn. Magn. Mater.* **2012**, *324*, 2051–2056. [CrossRef]
16. Jing, L.; Su, Z.; Wang, T.; Wang, Y.; Qu, R. Multi-objective optimization analysis of magnetic gear with HTS bulks and uneven Halbach arrays. *IEEE Trans. Appl. Supercond.* **2023**, *33*, 5202705. [CrossRef]
17. Zhu, Z.Q.; Howe, D. Halbach permanent magnet machines and applications: A review. *Inst. Electr. Eng. Proc. Electr. Power Appl.* **2001**, *148*, 299–308. [CrossRef]
18. Jing, L.; Liu, W.; Tang, W.; Qu, R. Design and optimization of coaxial magnetic gear with double-layer PMs and spoke structure for tidal power generation. *IEEE/ASME Trans. Mechatron.* **2023**, *28*, 3263–3271. [CrossRef]
19. Aloeyi, E.F.; Shoaei, A.; Wang, Q. A hybrid coaxial magnetic gear using flux-focusing halbach permanent magnet arrangement. In Proceedings of the 2023 IEEE 14th International Conference on Power Electronics and Drive Systems (PEDS), Montreal, QC, Canada, 7–10 August 2023; pp. 1–6.
20. Jian, L.; Chau, K.T. Analytical calculation of magnetic field distribution in coaxial magnetic gears. *Prog. Electromagn. Res.* **2009**, *92*, 1–16. [CrossRef]
21. Zhang, X.; Liu, X.; Wang, C.; Chen, Z. Analysis and design optimization of a coaxial surface-mounted permanent-magnet magnetic gear. *Energies* **2014**, *7*, 8535–8553. [CrossRef]
22. Jian, L.; Deng, Z.; Shi, Y.; Wei, J.; Chan, C.C. The mechanism how coaxial magnetic gear transmits magnetic torques between its two rotors: Detailed analysis of torque distribution on modulating ring. *IEEE/ASME Trans. Mechatron.* **2019**, *24*, 763–773. [CrossRef]
23. Spałek, D. Analytical electromagnetic field and forces calculation for linear, cylindrical and spherical electromechanical converters. *Bull. Pol. Acad. Sci. Tech. Sci.* **2004**, *52*, 239–250.
24. Niguchi, N.; Hirata, K. Cogging torque analysis of magnetic gear. *IEEE Trans. Ind. Electron.* **2011**, *59*, 2189–2197. [CrossRef]
25. Tzouganakis, P.; Gakos, V.; Kalligeros, C.; Tsolakis, A.; Spitas, V. Fast and efficient simulation of the dynamical response of coaxial magnetic gears through direct analytical torque modelling. *Simul. Model. Pract. Theory* **2023**, *123*, 102699. [CrossRef]
26. Lubin, T.; Mezani, S.; Rezzoug, A. Development of a 2-D analytical model for the electromagnetic computation of axial-field magnetic gears. *IEEE Trans. Magn.* **2013**, *49*, 5507–5521. [CrossRef]